

# Hyperfine level structure in nitrogen-vacancy centers near the ground-state level anticrossing

Marcis Auzinsh<sup>1</sup>, Andris Berzins<sup>1</sup>, Dmitry Budker<sup>2,3</sup>, Laima Busaite<sup>1,\*</sup>, Ruvin Ferber<sup>1</sup>, Florian Gahbauer<sup>1</sup>, Reinis Lazda<sup>1,†</sup>, Arne Wickenbrock<sup>2</sup>, and Huijie Zheng<sup>2,‡</sup>

<sup>1</sup>*Laser Centre, University of Latvia*

<sup>2</sup>*Helmholtz Institute Mainz, Johannes Gutenberg University and*

<sup>3</sup>*Department of Physics, University of California at Berkeley, USA*

Energy levels of the nitrogen-vacancy centers in diamond were investigated using optically detected magnetic-resonance spectroscopy near the electronic ground-state level anticrossing (GSLAC) at an axial magnetic field around 102.4 mT in diamond samples with low (1 ppm) and high (200 ppm) nitrogen concentration. By applying microwaves in the frequency ranges from 0 to 40 MHz and from 5.6 to 5.9 GHz, we observed transitions that involve eigenstates mixed by the hyperfine interactions. We developed a theoretical model that describes the level mixing, transition energies, and transition strengths between the ground-state sublevels, including coupling to the nuclear spin of the NV centers <sup>14</sup>N nucleus. The calculations were combined with the results from a fitting procedure that extracted information about the polarization of nuclear spin from the experimental curves using the model. These results are important for the optimization of experimental conditions in GSLAC-based applications, e.g., microwave-free magnetometry and microwave-free nuclear-magnetic-resonance probes.

PACS numbers: 76.30.Mi, 76.70.Hb, 75.10.Dg

## I. INTRODUCTION

Nitrogen-vacancy (NV) color centers in diamond crystals currently are used in a broad range of applications. They serve as qubits [1] or quantum-memory elements [2] for quantum computers, or probes for various physical properties like magnetic field [3], electric field [4], strain [5, 6], rotation [7–9] or temperature [10]. They can also be used to detect the properties of electronic and nuclear spins on the surface as well as inside the diamond crystal [11–14], such as substitutional nitrogen (P1) centers [15–17] or <sup>13</sup>C atoms. In these experiments usually the dephasing time  $T_2$  or the relaxation time  $T_1$  are measured directly. NV centers are also used to study spin-resonance related to cross-relaxation with other point defects in the diamond lattice [18].

For all these applications it is crucially important to know in detail the electronic structure of the NV center, including its hyperfine structure, which arises from the interaction of the electron spin with the nuclear spin of the <sup>14</sup>N atom which is a part of NV center. The energy levels split by the hyperfine interaction, can interact with an external magnetic field near the field values at which their magnetic sublevels cross or have avoided crossings (e.g., GSLAC). The contribution of the hyperfine interaction to these anticrossings has been studied experimentally and theoretically for interactions with the nuclear spin of <sup>13</sup>C [19, 20], <sup>14</sup>N [21–23], and <sup>15</sup>N [21, 24] and using a group-theory approach [25].

In this study we used the method of optically detected magnetic resonance (ODMR) [26] on the ground state  $m_s = 0 \rightarrow m_s = \pm 1$  transitions to study the hyperfine level structure of NV-center ensembles in the vicinity of the GSLAC. We obtained the hyperfine level structure and the transition strengths from the theoretical model. Then we used a parameter-optimization procedure to fit the experimentally measured curves with the results of a theoretical calculation.

This fitting procedure yielded information about the degree of nuclear polarization of the <sup>14</sup>N spin in the vicinity of the GSLAC.

## II. HYPERFINE LEVEL ANTICROSSING IN NV CENTERS IN DIAMOND

The NV center is composed of a substitutional nitrogen atom and an adjacent vacancy. It exists in different charged states NV<sup>0</sup> and NV<sup>-</sup>. In this work we focus on the energy levels of the NV<sup>-</sup> and refrain from writing out the charge state. The NV center has an electron spin  $S = 1$  in the ground state. There are both triplet and singlet excited states as shown in Fig. 1(a).

The NV center has a splitting between the ground-state magnetic sublevels of the electron spin  $m_S = 0$  and  $m_S = \pm 1$  even in the absence of an external magnetic field due to spin-spin interaction [27]. This zero-field splitting corresponds to 2870 MHz in the ground state and about 1400 MHz in the excited state. If an external magnetic field  $\mathbf{B}$  is applied along the NV axis, the magnetic sublevels of the electron spin acquire additional energy equal to

\*Electronic address: laima.busaite@lu.lv

†Electronic address: reinis.lazda@lu.lv

‡Electronic address: zheng@uni-mainz.de

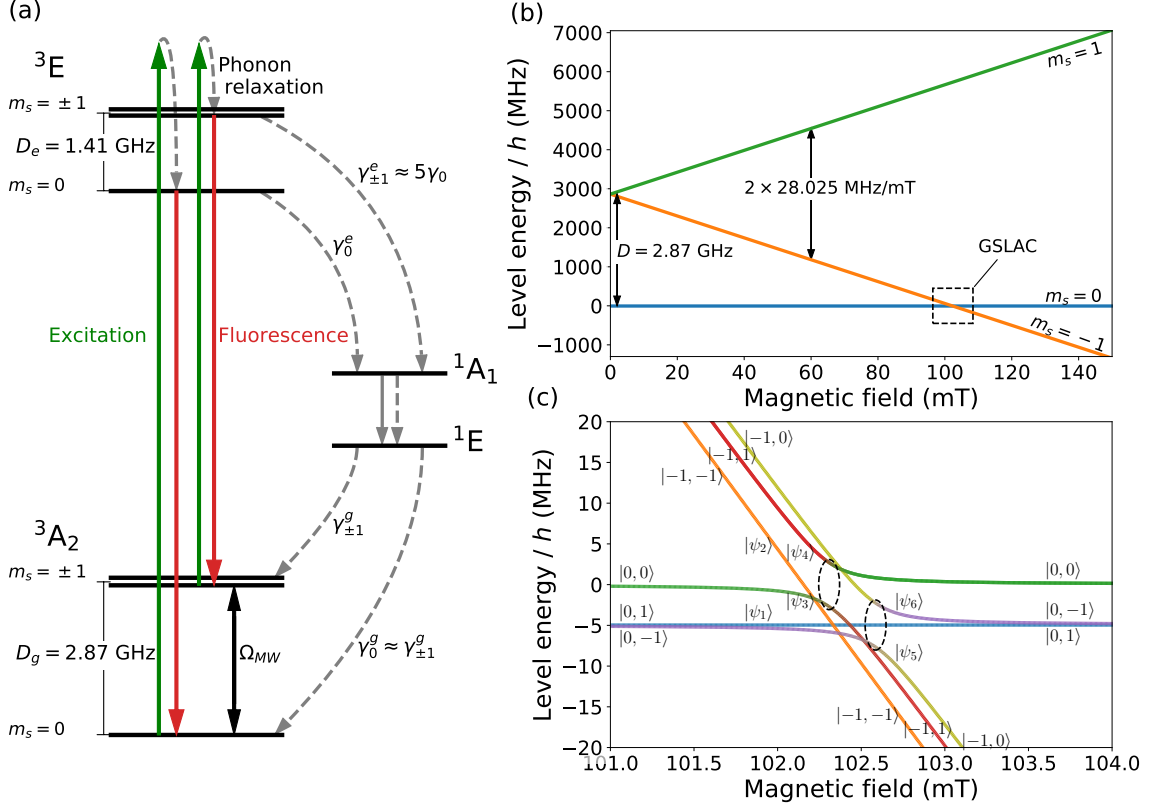


FIG. 1: (a) Level scheme for an NV center in diamond. (b) Level crossing of electron-spin magnetic sublevels in the ground state. (c) Hyperfine level ( $|m_S, m_I\rangle$ ) anticrossing in the vicinity of the GSLAC. The level of mixing near the GSLAC (denoted by the dashed ellipses) is indicated by the relative admixture of the colors in each curve; the lines corresponding to unmixed states do not change color.

$$\Delta E_{m_S} = \gamma_e B m_S, \quad (1)$$

where  $\gamma_e = 28.025$  GHz/T is the electron gyromagnetic ratio,  $m_S$  is the magnetic quantum number of the electron spin, and  $B$  is the magnetic field.

In addition to the electronic states,  $^{14}\text{N}$  has a nuclear spin  $I = 1$  which interacts with the NV electron spin. The Hamiltonian for the NV center including the hyperfine interaction with  $^{14}\text{N}$  in an external magnetic field  $\mathbf{B}$  along the  $z$ -axis (NV axis) can be written as [15]

$$\hat{H} = D\hat{S}_z^2 + \gamma_e \mathbf{B} \cdot \hat{\mathbf{S}} + \hat{\mathbf{S}} \cdot \hat{\mathbf{A}} \cdot \hat{\mathbf{I}} + Q\hat{I}_z^2 - \gamma_n \mathbf{B} \cdot \hat{\mathbf{I}}, \quad (2)$$

where  $D = 2870$  MHz is the zero-field splitting of the ground-state components with spin magnetic quantum numbers  $m_S = 0$  and  $m_S = \pm 1$ . The matrix  $\hat{\mathbf{A}}$  is a diagonal hyperfine-interaction tensor between the electron spin  $\mathbf{S}$  and nuclear spin  $\mathbf{I}$ ,

$$\hat{\mathbf{A}} = \begin{pmatrix} A_{\perp} & 0 & 0 \\ 0 & A_{\perp} & 0 \\ 0 & 0 & A_{\parallel} \end{pmatrix}, \quad (3)$$

where the hyperfine-interaction parameters are  $A_{\parallel} = -2.14$  MHz,  $A_{\perp} = -2.70$  MHz. The quadrupole interaction parameter  $Q = -4.96$  MHz, and the strengths of the nuclear spin interaction with the external magnetic field is determined by the gyromagnetic ratio of  $^{14}\text{N}$  nucleus  $\gamma_n = 3.077$  MHz/T. The values of the constants are taken from [15] and references therein.

A crossing between  $m_S = 0$  and  $m_S = -1$  occurs when the Zeeman splitting compensates the zero-field splitting at a magnetic field value of  $D/\gamma_e = 102.4$  mT [see Fig. 1(b)]. Owing to the hyperfine interaction, some of the energy levels exhibit avoided crossings or anticrossings [see Fig. 1(c)].

It is possible to ignore the contribution of the  $m_S = +1$  sublevel when calculating the eigenvalues and eigenvectors of the  $m_S = 0$  and  $m_S = -1$  components near the GSLAC since the  $m_S = +1$  sublevel is separated from the other two by an energy corresponding to 5740 MHz. Thus, we use a “truncated” Hamiltonian that only includes the electron spin sublevels with  $m_S = 0$  and  $m_S = -1$  and the corresponding nuclear spin sublevels with  $m_I = 0, \pm 1$ , to obtain approximate analytical solutions for the energy levels and wave functions of the hyperfine states. The energies  $E_i$  of these components

are

$$E_1 = Q, \quad (4a)$$

$$E_2 = A_{\parallel} - 2\mu_B B + D + Q, \quad (4b)$$

$$E_3 = \frac{1}{2} \left( -\sqrt{(A_{\parallel} + 2\mu_B B - D - Q)^2 + 4A_{\perp}^2} - A_{\parallel} - 2\mu_B B + D + Q \right), \quad (4c)$$

$$E_4 = \frac{1}{2} \left( \sqrt{(A_{\parallel} + 2\mu_B B - D - Q)^2 + 4A_{\perp}^2} - A_{\parallel} - 2\mu_B B + D + Q \right), \quad (4d)$$

$$E_5 = \frac{1}{2} \left( -\sqrt{4A_{\perp}^2 + (2\mu_B B - D + Q)^2} - 2\mu_B B + D + Q \right), \quad (4e)$$

$$E_6 = \frac{1}{2} \left( \sqrt{4A_{\perp}^2 + (2\mu_B B - D + Q)^2} - 2\mu_B B + D + Q \right). \quad (4f)$$

The wave functions can be written in the uncoupled basis  $|m_S, m_I\rangle$  as follows:

$$|\psi_1\rangle = |0, 1\rangle, \quad (5a)$$

$$|\psi_2\rangle = |-1, -1\rangle, \quad (5b)$$

$$|\psi_3\rangle = \frac{1}{|\alpha_1|} |-1, 1\rangle - \frac{1}{|\alpha_1|} \left( \kappa_1 + \sqrt{\kappa_1^2 + 1} \right) |0, 0\rangle, \quad (5c)$$

$$|\psi_4\rangle = \frac{1}{|\alpha_1|} |-1, 1\rangle - \frac{1}{|\alpha_1|} \left( \kappa_1 - \sqrt{\kappa_1^2 + 1} \right) |0, 0\rangle, \quad (5d)$$

$$|\psi_5\rangle = \frac{1}{|\alpha_2|} |-1, 0\rangle - \frac{1}{|\alpha_2|} \left( \kappa_2 + \sqrt{\kappa_2^2 + 1} \right) |0, -1\rangle, \quad (5e)$$

$$|\psi_6\rangle = \frac{1}{|\alpha_2|} |-1, 0\rangle - \frac{1}{|\alpha_2|} \left( \kappa_2 - \sqrt{\kappa_2^2 + 1} \right) |0, -1\rangle, \quad (5f)$$

where

$$\kappa_1 = \frac{D + Q - A_{\parallel} - 2\mu_B B}{2A_{\perp}}, \quad (6a)$$

$$\kappa_2 = \frac{D - Q - 2\mu_B B}{2A_{\perp}} \quad (6b)$$

and

$$|\alpha_{1,2}| = \sqrt{\left( \kappa_{1,2} + \sqrt{\kappa_{1,2}^2 + 1} \right)^2 + 1}. \quad (7)$$

In an axially symmetric magnetic field,  $m_S$  and  $m_I$  are good quantum numbers, and only states with equal total electron and nuclear spin projections  $m_S + m_I$  are mixed. Consequently, two states from this manifold, in our notation  $\psi_1$  and  $\psi_2$ , remain unmixed even in a strong

magnetic field. The remaining four states form two pairs of mixed states. One pair consists of states  $\psi_3$  and  $\psi_4$ , the other of states  $\psi_5$  and  $\psi_6$ . This information about the state mixing will be important when we analyze which transitions are allowed and which are forbidden when the

magnetic field value is close to 102.4 mT.

Magnetic-dipole transitions between various states can be driven with an applied microwave field. The selection rules for these transitions are simple, namely,  $\Delta m_S = \pm 1$  and  $\Delta m_I = 0$  [28].

In order to calculate the transition probabilities for these transitions, we write the Hamiltonian for magnetic dipole transitions with raising and lowering operators

$$\hat{H}^{(m)} = \frac{1}{2} (\hat{S}_+ + \hat{S}_-), \quad (8)$$

where

$$\hat{S}_\pm = \hat{S}_x \pm i\hat{S}_y, \quad (9)$$

and the  $\hat{S}_{x,y}$  are the Pauli matrices for  $J = 1$ . Then we change to the  $\hat{S}'$  basis using the ground-state eigenvectors  $|\psi_i\rangle$  of the Hamiltonian from (2):

$$\hat{S}'_\pm = \Psi^\dagger [\hat{S}_\pm \otimes \mathbf{1}(3)] \Psi. \quad (10)$$

The columns of the matrix  $\Psi$  are the ground-state eigenvectors  $|\psi_i\rangle$ , and  $\mathbf{1}(3)$  is the  $3 \times 3$  identity matrix. Now we rewrite the magnetic dipole Hamiltonian in this basis:

$$\hat{H}'^{(m)} = \frac{1}{2} (\hat{S}'_+ + \hat{S}'_-) = \begin{pmatrix} d'_{00} & d'_{0-1} & d'_{01} \\ d'_{-10} & d'_{-1-1} & d'_{-11} \\ d'_{10} & d'_{1-1} & d'_{11} \end{pmatrix} \otimes \mathbf{1}(3). \quad (11)$$

And then the transition probability is

$$p'_{ij} = d'_{ij} \cdot d'_{ji}. \quad (12)$$

### III. EXPERIMENTAL SET-UP

The NV centers were optically pumped with a green 532 nm Nd:YAG laser (Coherent Verdi) and optically polarized to the  $m_S = 0$  state, while near-infrared fluorescence from the  ${}^3E$  state was monitored [see the transition diagram in Fig. 1(a)]. Following the ODMR method, a microwave field was applied to induce transitions between the ground-state sublevels that were continuously pumped to the  $m_S = 0$  state. When a MW field is on resonance with a transition from  $m_S = 0$  to  $m_S = \pm 1$ , the fluorescence intensity decreases. As a result, the hyperfine level structure can be probed by observing the fluorescence intensity as a function of MW frequency.

We measured ODMR signals from ensembles of NV centers in two different diamond samples. One sample was a dense high-pressure, high-temperature (HPHT) crystal with a relatively high concentration of nitrogen of around 200 ppm. The other sample was produced by chemical vapor deposition (CVD) with a more dilute concentration of nitrogen of around 1 ppm. The measurements with the dense sample were performed at the University of Latvia in Riga, and measurements with the dilute sample, at the Johannes Gutenberg-University in Mainz.

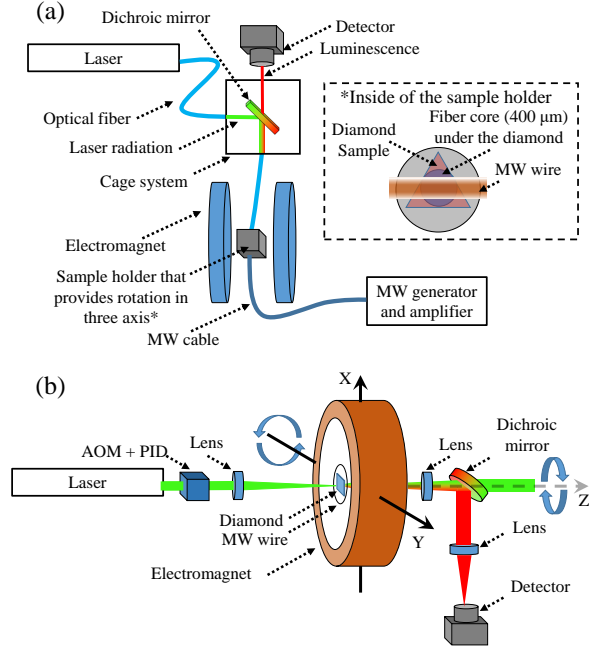


FIG. 2: **(a)** Riga setup. The laser light was coupled into a fiber that led it to a cage-system cross, in which a dichroic mirror (Thorlabs DMLP567R) reflects the green light, that in turn was coupled into another fiber that led to the sample. A small portion of the green light that passed through the dichroic mirror was used to monitor the laser power. The fluorescence from the sample, which was glued to the end of the fiber, was collected with the same fiber, and, after passing through the dichroic mirror and a long-pass filter (Thorlabs FEL0600), it was focused onto a photodiode with an amplifier (Thorlabs PDA36A-EC). **(b)** Mainz setup. The laser light was focused on the sample by using a lens, fluorescence was collected and measured with a photodetector (Thorlabs APD410A/M). The diamond sample is located at the center of the magnet bore. The rotation axes of the sample and the electromagnet are depicted with blue arrows.

Figure 2(a) shows the experimental setup used in Riga. The magnetic field was produced by a custom-built magnet initially designed for electron paramagnetic resonance (EPR) experiments. It consists of two 19 cm diameter iron poles with a length of 13 cm each, separated by a 5.5 cm air gap. This magnet could provide a highly homogeneous field (0.0002 mT over the sensing volume (estimated by COMSOL modeling)). The diamond sample under investigation was held in place using a nonmagnetic holder (custom-made by STANDA), which provided three axes of rotation to align the NV axis with the applied magnetic field. Light with a wavelength of 532 nm (Coherent Verdi Nd:YAG) was delivered to the sample via an optical fiber with a core diameter of 400 micrometers (numerical aperture of 0.39). The same fiber was used to collect red fluorescence light, which was separated from the residual green reflections by a dichroic

mirror and a long-pass filter (Thorlabs DMLP567R and FEL0600) and focused onto an amplified photodiode (Thorlabs PDA36A-EC). The signals were recorded and averaged on a digital oscilloscope (Agilent DSO5014A or Yokogawa DL6154) or a DAQ card (Measurement Computing USB-1408FS).

Figure 2(b) shows the experimental setup used for the low-density sample in Mainz. A custom-made electromagnet was used with 200 turns wound on a water-cooled copper mount. The electromagnet produced a field of 2.9 mT/A. In this setup the diamond could be rotated around the z-axis (NV axis). Moreover, the electromagnet can be moved with a computer-controlled 3D translation stage (Thorlabs PT3-Z8) and a rotation stage (Thorlabs NR360S, y-axis). In this way, all degrees of freedom for centering the diamond in the magnet and aligning the NV axis to the magnetic field were available. In this setup an AOM was used in combination with a photodiode and PID to stabilize the laser intensity.

In both setups, the microwave field was generated and amplified using two sets of devices depending on the required frequency range. In Riga, for low frequencies a TTI TG5011 generator (0.001 MHz to 50 MHz) and for high frequencies a function generator (SRS SG386) with a power amplifier (Minicircuits ZVE-3W-83+) provided up to +30dBm. In Mainz, an SRS SG386 was used as a function generator over the entire range, in conjunction with power amplifiers. At high frequencies, an RFLU PA0706GDRF amplifier (Lambda) was used. It was replaced at low frequencies with a (Minicircuits ZHL-32A+) amplifier.

#### IV. EXPERIMENTAL RESULTS AND ANALYSIS

##### A. ODMR signals for transitions to the $|m_s = +1\rangle$ sublevel

Figure 3 depicts ODMR signals for transitions in the frequency range 5.6–5.9 GHz, where the microwave field is resonant with transitions from the  $m_s = 0$  and  $m_s = -1$  hyperfine levels, which are partially mixed, to the  $m_s = +1$  hyperfine level [see Fig. 1(b)]. Experimentally measured signals are depicted together with curves obtained from a model calculation with some parameters obtained from a fitting procedure as explained below. Figures 3(a)–(c) depict magnetic sublevels at a given magnetic field and indicate the allowed microwave transitions as arrows. The wave functions  $|\psi_1\rangle$ – $|\psi_6\rangle$  are given in Eq. (5). In this transition, additionally the states  $|m_s = +1, m_I = +1\rangle$ ,  $|m_s = +1, m_I = -1\rangle$ , and  $|m_s = +1, m_I = 0\rangle$  participate, which are labeled as  $|\psi_7\rangle$ ,  $|\psi_8\rangle$ , and  $|\psi_9\rangle$ , respectively. The middle row [Figures 3(d)–(f)] shows signals obtained with the 200 ppm sample and the bottom row [Figures 3(g)–(i)], signals obtained with the 1 ppm sample.

We used a parameter-optimization procedure based on

a  $\chi^2$  test to determine the contribution of each transition in Fig. 3(a)–(c) to the overall lineshapes in Fig. 3(d)–(i). To illustrate the procedure, let us consider Fig. 3(g). This signal was recorded at a magnetic field value far away from the GSLAC. As a result, the mixing of the sublevels is insignificant, and contributions are expected only from the following three transitions:  $|0, 1\rangle \rightarrow |-1, 1\rangle$  (blue),  $|0, -1\rangle \rightarrow |-1, -1\rangle$  (purple), and  $|0, 0\rangle \rightarrow |-1, 0\rangle$  (green). In these transitions between electronic states, the nuclear spin projection  $m_I$  does not change. We assumed that each transition has a Lorentzian lineshape centered at its respective transition frequency, which follows from the level energies in Eq. (4). The transition strengths for these three transitions are equal, which is indicated by the fact that all three arrows have the same transparency. Nevertheless, the relative contributions (peak amplitudes) of each transition may differ because of differences in the populations of the three ground states involved:  $|0, +1\rangle$ ,  $|0, 0\rangle$ , and  $|0, -1\rangle$ , corresponding to the distribution of the nuclear spin projections  $m_I$ .

There are multiple ways of fitting the measured data to find the distribution of spin values, for example, one can use the spin temperature [29] method or a multipole expansion method [30] which we have used here, described below.

We characterized the effects of a nuclear spin distribution among its three possible values by modifying the identity matrix in (10) in order to enhance the probability of transitions from the sublevel with  $m_I = 1$  with respect to the other two sublevels. Concretely,

$$\mathbf{1}' = \begin{pmatrix} 1 & 0 & 0 \\ 0 & 1 - q_1 & 0 \\ 0 & 0 & 1 - q_2 \end{pmatrix}, \quad (13)$$

where the two parameters  $q_1$  and  $q_2$  characterized the distribution of nuclear polarization and could take on values between zero and unity.

Next we attempted to find the set of parameters  $\{q_1, q_2, B\}$  that minimized the  $\chi^2$  value for the hypothesis that our theoretical model with these parameters described the measured data. The magnetic field value  $B$  was allowed to vary over a small range since the position of the ODMR peak depends not only on  $B$ , but also on the distribution of nuclear spin values, even far away from the GSLAC. In this way, a calibration curve for  $B$  as a function of magnet current was obtained. This curve was used instead of the parameter search procedure for magnetic field values within  $\pm 0.5$  mT of the actual GSLAC position.

For each possible set of parameters, we calculated the corresponding populations of the eigenstates in (5). From these states, we could obtain the transition strengths. The amplitude of each transition peak is proportional to product of the transition strength and the population of the relevant lower state (the  $m_s = 1$  states are assumed “empty”). Then we used the SciPy optimize function [31] to determine the widths of the Lorentzians corresponding to each of the hyperfine transition peaks. This step

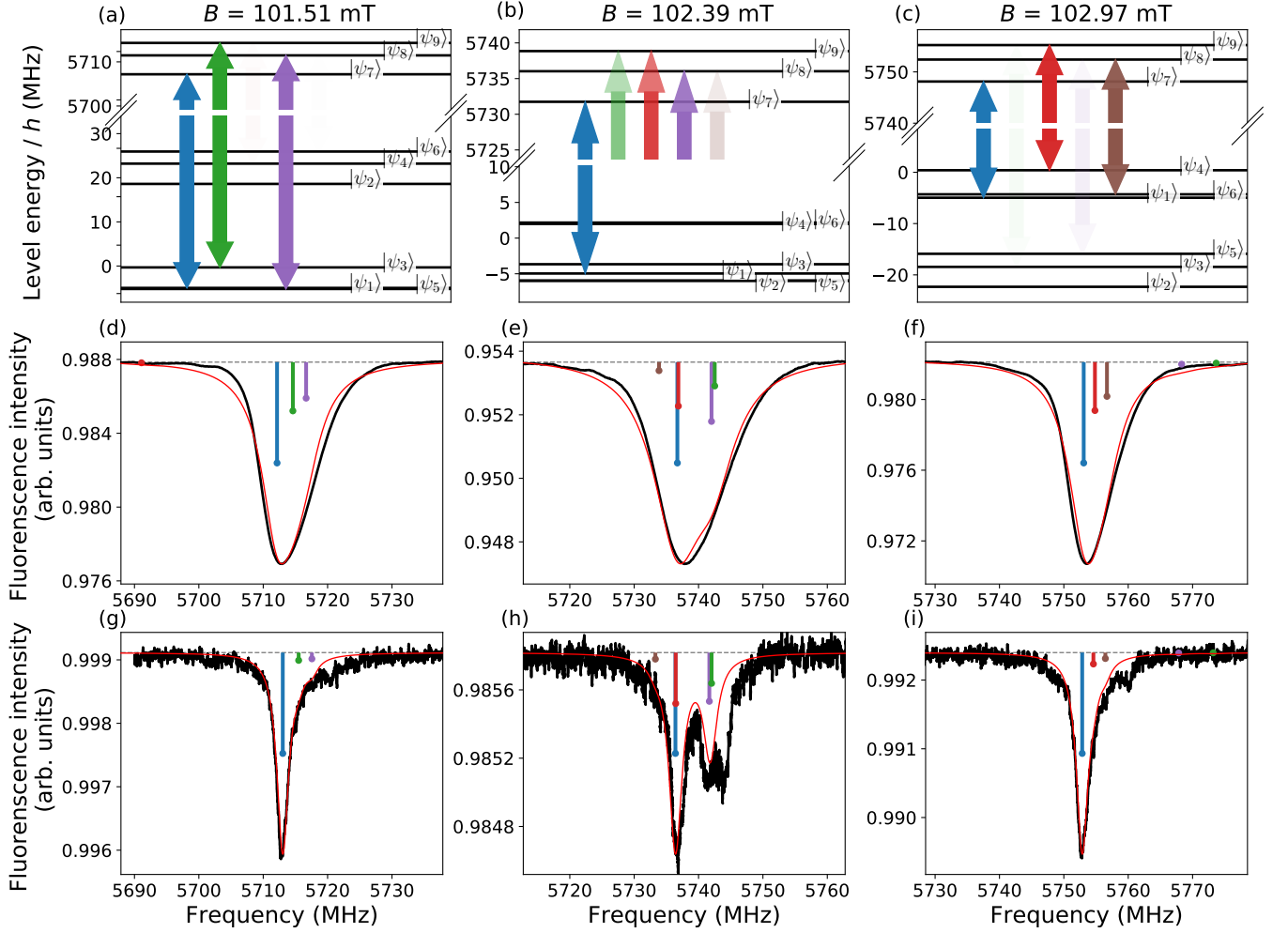


FIG. 3: ODMR signals at high microwave field frequencies. The top row (a)–(c) shows the transitions between respective levels (Eqn. (5)). In the middle row (d)–(f), black lines show experimental signals for the 200 ppm sample, and in the bottom row (g)–(i), the black lines show experimental signals for the 1 ppm sample. The red lines in (d)–(i) show the results of the theoretical calculations with the parameters from the fitting procedure described in the text. The colored arrows in (a)–(c) show the possible transitions with the transition strength indicated by the level of transparency. The vertical bars in (d)–(i) correspond to the transitions depicted by the arrows in (a)–(c) of the same color and their length determines the contribution to the overall lineshape of that transition, which is proportional to the product of the level population and the transition strength.

was important because the width of the Lorentzians for the 1 ppm sample is around 1 MHz and about two times larger for the 200 ppm sample. At the GSLAC the width of the Lorentzians increases due to increased relaxation rates arising from increased interaction between the hyperfine levels [15].

We calculated the  $\chi^2$  value using this set of parameters. We repeated the procedure for the next set of parameters and stored those that yielded the smallest  $\chi^2$  value. The peak amplitudes thus obtained are shown as the length of the colored bars in the Fig. 3(g). The color of each bar corresponds to the color of the arrow that represent the corresponding transition in Fig. 3(a). We proceeded in a similar fashion for all subfigures. Near the GSLAC, there are more possible transitions that must

be considered as a result of sublevel mixing (as it follows from Eqn. (5)–(7)). The number of possible transitions and their relative transition strengths are indicated by the number of arrows in Fig. 3(b) and their transparency levels.

### B. ODMR signals for the $|m_S = 0\rangle \rightarrow |m_S = -1\rangle$ transition

We also measured ODMR signals for the  $|m_S = 0\rangle \rightarrow |m_S = -1\rangle$  transition within  $\pm 1.5$  mT of the GSLAC, which corresponds to microwave frequencies below 40 MHz, and some results are shown in Fig. 4. Experimentally measured signals are plotted together with signals

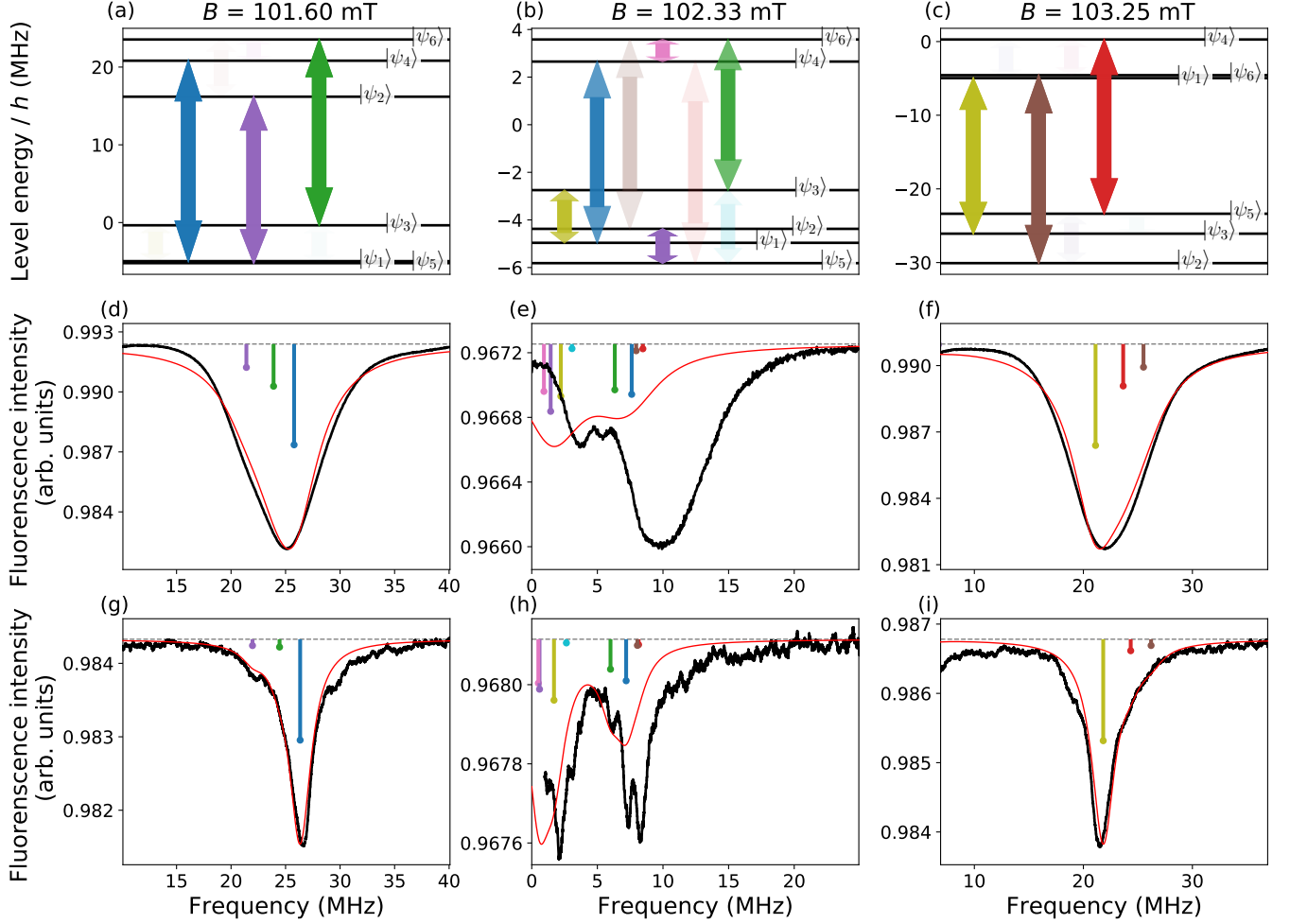


FIG. 4: ODMR signals at low microwave field frequencies. The top row (a)–(c) shows the transitions between respective levels (Eqn. (5)). In the middle row (d)–(f), black lines show experimental signals for the 200 ppm sample, and in the bottom row (g)–(i), the black lines show experimental signals for the 1 ppm sample. The red lines in (d)–(i) show the results of the theoretical calculations with the parameters from the fitting procedure described in the text.

from a model calculation using parameters that were obtained in a similar way as in Sec. IV A, except right at the GSLAC. For the 200 ppm sample, the fitting procedure broke down for magnetic-field values within  $\pm 0.5$  mT of the GSLAC. Therefore, in Fig. 4(e) we used the nuclear spin population distribution and peak widths obtained at the corresponding magnetic field value for the high-frequency case (Sec. IV A). The top row (a)–(c) shows the magnetic-sublevel structure in a particular magnetic field with the allowed transitions depicted with arrows whose transparency indicates the relative transition strength. The middle row (d)–(f) shows measured signals in the 200 ppm sample. The bottom row (g)–(i) shows signals measured in the 1 ppm sample. Again, above and below the GSLAC, the signals consist of three components, which correspond to the allowed transitions between hyperfine levels that are weakly mixed in the magnetic field, but at the GSLAC, there is strong mixing and more transitions

must be taken into account, as indicated by the number of arrows in Fig. 4(b). Above and below the GSLAC, the agreement between measured and calculated curves is quite good. However, right near the GSLAC there are large discrepancies: amplitude and center frequencies of the peaks do not agree. Possible reasons for the discrepancy might be a lack of microwave power, inhomogeneities in the diamond or in the magnetic field, or interactions with other nearby spins, such as P1 centers or  $^{13}\text{C}$  nuclei, that were not included in our model.

Another reason for the discrepancy might be additional interactions that are not taken into account in the Hamiltonian in Eq. (2). As a result, some levels that are currently unmixed and should cross, instead would undergo anticrossing. Thus, there would be a nonzero minimum transition frequency where our model would predict that the transition frequency should approach zero near the crossing point. In fact, one could estimate the strength of



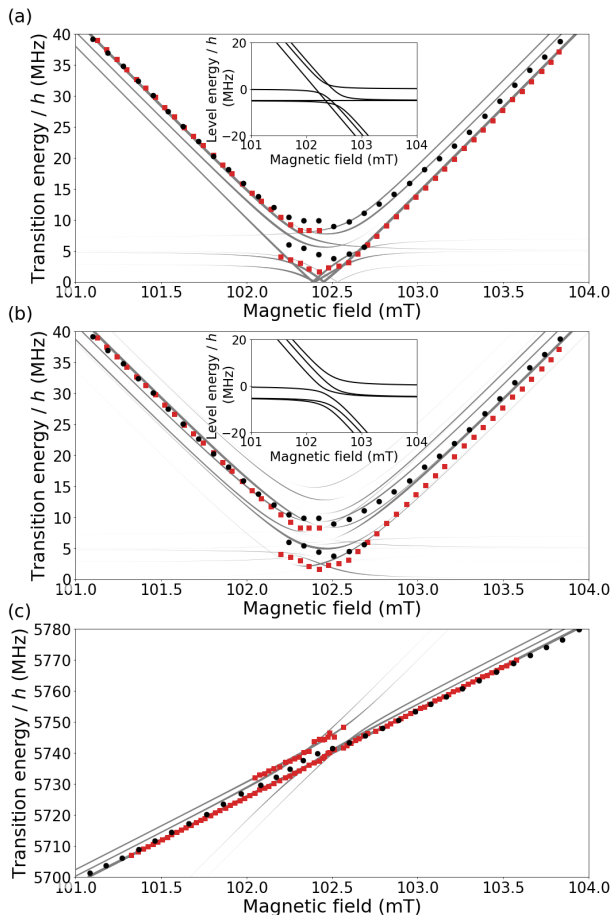


FIG. 5: Calculated and observed positions of the ODMR signal peaks. The solid line depicts calculated positions. The width of the line indicates relative intensity of the peak. Black dots mark the observed positions of the ODMR signal peak from the 200 ppm sample, while red squares mark the observed positions of the ODMR signal peak from the 1 ppm sample. (a) shows the results for the  $|m_S = 0\rangle \rightarrow |m_s = -1\rangle$  transition in the case of the NV center's axis being parallel to the magnetic field vector. (b) depicts the same signal when there is an angle of 0.1 degrees between the NV axis and the magnetic field vector, which corresponds to a transverse magnetic field of 0.18 mT. (c) shows the  $|m_S = 0\rangle \rightarrow |m_s = +1\rangle$  transition (see Fig. 3.).

the unknown interaction from the lowest peak frequency in a sweep of magnetic field values through the GSLAC. This minimum peak frequency would correspond to the closest approach of two levels in an anticrossing and thus indicate the interaction strength.

One effect that could introduce mixing in the Hamiltonian and convert crossings into anticrossings is a transversal magnetic field (introducing an angle between the leading field and the NV axis). Figure 5 shows the change of transition probabilities in the case of a small deviation from the “ideal” geometry. Figure 5(a) depicts the position of the maxima of the ODMR signal at a se-

ries of different magnetic field values. As expected, the calculated signal approaches zero frequency right at the crossing point of levels  $\psi_2$  and  $\psi_5$  at 102.45 mT and at the crossing point of levels  $\psi_1$  and  $\psi_3$  at 102.5 mT [see Fig. 1(c)]. However, when a small angle equal to 0.1 degrees is introduced between the NV axis and the magnetic field vector, which corresponds to a transverse magnetic field of 0.18 mT, the levels that initially underwent crossings now are mixed by the transverse magnetic field and instead undergo anticrossing (see inserts in Fig. 5). As a result the calculated signal peak positions no longer reach zero frequency [see Fig. 5(b)]. In Fig. 5(b), the calculated and observed positions of the ODMR peaks match rather well as they do also for the  $|m_S = 0\rangle \rightarrow |m_s = +1\rangle$  transition shown in Fig. 5(c).

We systematically performed a number of ODMR measurements at low frequencies for a range of magnetic field values near the GSLAC. Figures 6(a) and (b) show ODMR signals measured near the GSLAC with the 200 ppm sample, and Fig. 6(c) shows signals measured with the 1 ppm sample. The black curve shows the experimentally measured signals, while the red curve represents the result of the theoretical model calculation with parameters obtained by the same fitting procedure as described in connection with Fig. 4. Again, the nuclear spin populations and peak widths within  $\pm 0.5$  mT of the GSLAC were taken from the values obtained for the high-frequency case at the same magnetic field value. Everywhere else the parameter optimization procedure was used as described in Sec. IV A. The experimental data in Fig. 6(a) and Fig. 6(b) are identical, but for the calculated curves, the NV axis and the magnetic field vector were assumed to be parallel in the former case, whereas in the latter, an angle  $\theta = 0.1$  degrees between the NV axis and the magnetic field direction was assumed. This angle was found to give the best overall agreement between the experimentally measured values and the curves obtained from the model calculations with parameter fitting.

In all these experimentally measured signals, the relative peak intensities were normalized separately for each magnetic field value, because at the GSLAC, the contrast of the signals decreased strongly in both samples, as shown in Fig. 7. The decrease in contrast near the GSLAC is caused by energy level mixing, which redistributes the population, resulting in fewer NV centers in the ground state available for MW transitions. The vertical bars depict calculated ODMR peak positions and relative intensities. It can be seen that below and above the GSLAC the measured and calculated signals agree rather well. However, right at the GSLAC the agreement is not as good, especially for the 200 ppm sample.

### C. Nuclear spin polarization

The peak amplitudes from the fit in Fig. 4(d)–(i), Fig. 6, and Fig. 3(d)–(i) contain information about the relative populations of the ground-state sublevels and



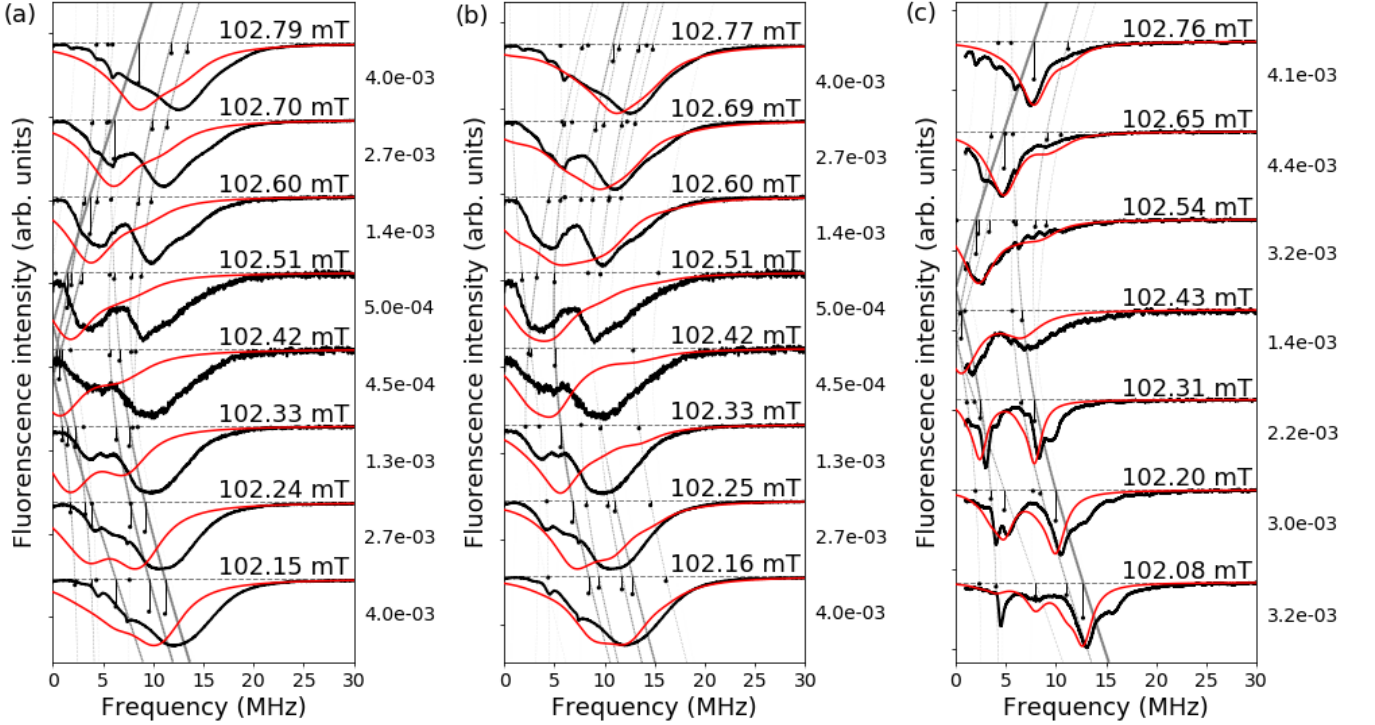


FIG. 6: Experimental signals (black) with theoretical calculations (red) for ground state  $m_S = 0 \rightarrow m_S = -1$  microwave transitions for different magnetic-field values. Experimental signal from the 200 ppm sample with the calculated signal for an angle between the NV axis and the magnetic field  $\mathbf{B}$  of (a)  $\theta = 0^\circ$  and (b)  $\theta = 0.1^\circ$  (transverse magnetic field 0.18 mT). (c) Experimental signal from the 1 ppm sample with the calculated signal at  $\theta = 0^\circ$ . Bars with black dots on one end are placed at the values of the transition frequencies for a specific magnetic-field value, and their length represents the calculated transition probability. For better readability, signals are arranged in order of descending magnetic field, and each curve is normalized separately with its relative intensity depicted at the right side of the graph.

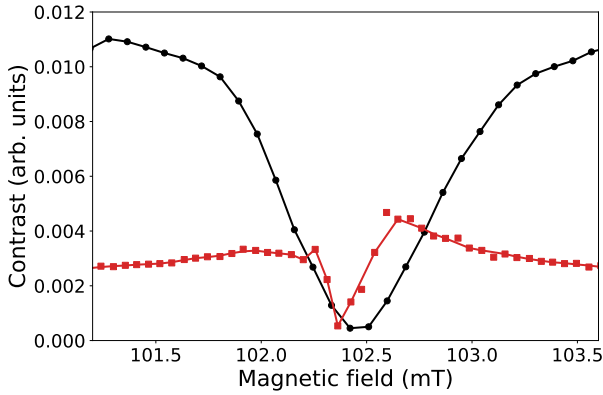


FIG. 7: ODMR signal contrast for the 1 ppm (red squares) and 200 ppm (black dots) sample for different magnetic field values. The image shows how the ODMR signal contrast changes close to the GSLAC region for the  $m_S = 0 \rightarrow m_S = -1$  transition (FIG. 6).

thus the nuclear spin polarization [19, 24, 32–38]. Nuclear spin polarization arises from an interplay of op-

tical pumping and sublevel mixing. Figure 1(c) shows how the  $|m_S = 0, m_I = -1\rangle$  sublevel is mixed with the  $|m_S = -1, m_I = 0\rangle$  sublevel near the GSLAC, where they are nearly degenerate. Optical pumping in this situation tends to move population from the  $|m_S = 0, m_I = -1\rangle$  sublevel to the  $|m_S = 0, m_I = 0\rangle$  sublevel via the  $|m_S = -1, m_I = 0\rangle$  sublevel. In a similar way, because of the mixing between  $|m_S = 0, m_I = 0\rangle$  sublevel and the  $|m_S = -1, m_I = +1\rangle$  sublevel, population moves from the  $|m_S = 0, m_I = 0\rangle$  sublevel to the  $|m_S = 0, m_I = +1\rangle$  sublevel via the  $|m_S = -1, m_I = +1\rangle$  sublevel. However, the  $|m_S = 0, m_I = +1\rangle$  sublevel is not mixed with any sublevel, and so the population tends to accumulate here, with the nuclear spin polarized to  $m_I = +1$ .

The nuclear spin polarization can be characterized using multipole expansion [30], in which the zero rank multipole moment (monopole  $\rho_0^0$ ) corresponds to population, the first rank moment (dipole moment  $\rho_0^1$ ), to orientation, and the second rank moment (quadrupole moment  $\rho_0^2$ ), to alignment. Due to continuous laser excitation and continuous action of the MW field in our system only longitudinal (along the magnetic field direction)  $\rho_0^1$  and  $\rho_0^2$  spin polarization components are created. At these conditions all the transverse (perpendicular to the the

magnetic field direction) components are equal to zero  $\rho_{\pm 1}^1 = 0$ ,  $\rho_{\pm 1}^2 = 0$ ,  $\rho_{\pm 2}^2 = 0$ .

Based on the component intensities, orientation would be written as

$$P_0^1 = \frac{\rho_0^1}{\rho_0^0} = \sqrt{\frac{3}{2}} \frac{n_{01} - n_{0-1}}{n_{01} + n_{00} + n_{0-1}}, \quad (14)$$

where  $n_{m_S m_I}$  is the sum of the component intensities of all transitions from level  $|m_S m_I\rangle$  (5).

Alignment can be calculated in a similar way as

$$P_0^2 = \frac{\rho_0^2}{\rho_0^0} = \sqrt{\frac{1}{2}} \frac{n_{01} + n_{0-1} - 2n_{00}}{n_{01} + n_{00} + n_{0-1}}. \quad (15)$$

Figures 8 and 9 show the degree of spin polarization as a function of magnetic field. The populations of the nuclear spin components were obtained from the peak amplitudes obtained by the parameter fitting procedure described in Sec. IV A, and then the orientation and alignment were calculated using Eqs. (14) and (15), respectively. The data for this procedure are shown in Fig. 3, supplemented by similar measurements at many more magnetic-field values. The population of each nuclear spin component is proportional to the corresponding peak amplitude divided by the transition strength. In both figures, the region at the center shaded in gray indicates the magnetic field values for which the model was found to be insufficient to produce the experimental signals adequately [see, for example, Fig. 3(h)]. The polarization values extracted by our method are plotted in this region as well, but they should be taken with caution. Both figures show nuclear polarization near the GSLAC with a minimum at the GSLAC position. For the 200 ppm sample, the features are broader than in the case of the 1 ppm sample. This difference could be attributed to higher relaxation rates in the 200 ppm sample. In principle, the polarization should vanish far away from the GSLAC where there is no mixing [24]. However, we did not observe this behavior over the measured range of magnetic field values.

## V. CONCLUSIONS

In this study we have observed microwave-induced transitions between the hyperfine components of the  $^3A_2$  ground-state sublevels of the NV center in diamond using the ODMR technique in two samples: a dilute sample with a nitrogen concentration of 1 ppm (in Mainz, Germany) and a denser sample with a nitrogen concentration of 200 ppm (in Riga, Latvia). We have developed a straightforward theoretical model to describe these ODMR signals. This model agrees with observations everywhere apart for magnetic field values within  $\pm 0.5$  mT of the GSLAC position, where the model was found to be insufficient for describing all observed features of the ODMR signal. For the range of magnetic field values in which the model works, it can be used

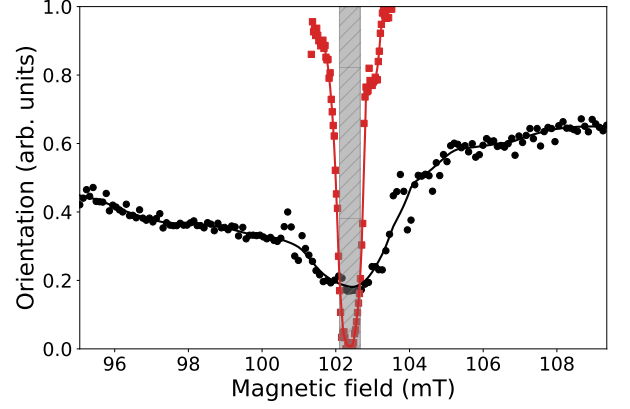


FIG. 8: Nuclear  $^{14}\text{N}$  spin orientation obtained for the ground state  $m_S = 0 \rightarrow m_S = +1$  transition from the fitted transition peak amplitudes. The red squares correspond to the 1 ppm sample and the black dots to the 200 ppm sample. The gray, shaded region corresponds to the magnetic field range in which the theoretical model does not reproduce the measurements well.

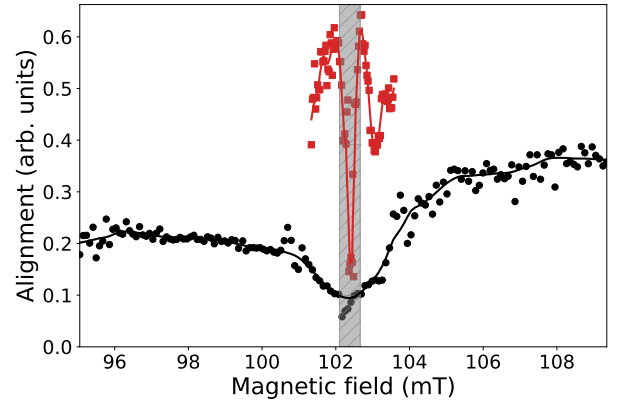


FIG. 9: Nuclear  $^{14}\text{N}$  spin alignment obtained for the ground state  $m_S = 0 \rightarrow m_S = +1$  transition from the fitted transition peak amplitudes. The red squares correspond to the 1 ppm sample and the black dots to the 200 ppm sample. The gray, shaded region corresponds to the magnetic field range in which the theoretical model does not reproduce the measurements well.

to measure the nuclear spin polarization of  $^{14}\text{N}$ , which we have demonstrated in this study. We have performed ODMR measurements on the  $|m_S = 0\rangle \rightarrow |m_S = -1\rangle$  transition as well as on the  $|m_S = 0\rangle \rightarrow |m_S = +1\rangle$  transition. The latter transition is somewhat simpler, since the  $|m_S = +1\rangle$  level is not involved in the anti-crossing and thus serves as a useful cross-check. The ODMR technique has proven to be a useful tool for investigating how the hyperfine interaction influences the energy-level structure near the GSLAC and, with further improvements to the theoretical model, could shed more light on additional interactions and the process of nuclear

polarization near the GSLAC.

## VI. ACKNOWLEDGEMENTS

The Riga group gratefully acknowledges the financial support from the M-ERA.NET project Metrology at the Nanoscale with Diamonds (MyND), from the Laserlab-Europe Project (EU-H2020 654148), and from the Base/Performance Funding Project Nr. AAP2016/B013,

ZD2010/AZ27. A. Berzins acknowledges support from the PostDoc Latvia Project Nr. 1.1.1.2/VIAA/1/16/024 "Two-way research of thin-films and NV centres in diamond crystal".

The Mainz group acknowledges support by the German Federal Ministry of Education and Research (BMBF) within the Quantumtechnologien program (FKZ 13N14439) and the DFG through the DIP program (FO 703/2-1). H. Zheng acknowledges support from the GRK Symmetry Breaking (DFG/GRK 1581) program.

- 
- [1] G. Popkin. *Science*, 354(6316):1090–1093, 2016.
  - [2] K. Heshami, D. G. England, P. C. Humphreys, P. J. Bustard, V. M. Acosta, J. Nunn, and B. J. Sussman. *Journal of Modern Optics*, 63(20):2005–2028, 2016.
  - [3] H. Zheng, G. Chatzidrosos, A. Wickenbrock, L. Bougas, R. Lazda, A. Berzins, F. H. Gahbauer, M. Auzinsh, R. Ferber, and D. Budker. Level anti-crossing magnetometry with color centers in diamond. In *Society of Photo-Optical Instrumentation Engineers (SPIE) Conference Series*, volume 10119 of *Society of Photo-Optical Instrumentation Engineers (SPIE) Conference Series*, page 101190X, February 2017.
  - [4] F. Dolde, H. Fedder, M. W. Doherty, T. Nbauer, F. Rempp, G. Balasubramanian, T. Wolf, F. Reinhard, L. C. L. Hollenberg, F. Jelezko, and J. Wrachtrup. *Nature Physics*, 7:459–463, 2011.
  - [5] Ph. Tamarat, N. B. Manson, J. P. Harrison, R. L. McMurtrie, A. Nizovtsev, C. Santori, R. G. Beausoleil, P. Neumann, T. Gaebel, F. Jelezko, P. Hemmer, and J. Wrachtrup. *New J. Phys.*, 10:045004, 2008.
  - [6] N. B. Manson, J. P. Harrison, and M. J. Sellars. *Phys. Rev. B*, 74:104303, 2006.
  - [7] M. Ledbetter, K. Jensen, R. Fischer, A. Jarmola, and D. Budker. *Phys. Rev. A*, 86:052116, 2012.
  - [8] A. A. Wood, E. Lilette, Y. Y. Fein, N. Tomek, L. P. McGuinness, L. C. L. Hollenberg, R. E. Scholten, and A. M. Martin. Quantum measurement of a rapidly rotating spin qubit in diamond. *ArXiv e-prints*, February 2018.
  - [9] A. Ajoy and P. Cappellaro. *Phys. Rev. A*, 86:062104, 2012.
  - [10] H. Clevenson, M. E. Trusheim, C. Teale, T. Schrder, D. Braje, and D. Englund. *Nature Physics*, 11:393–397, 2015.
  - [11] H. J. Mamin, M. Kim, M. H. Sherwood, C. T. Rettner, K. Ohno, D. D. Awschalom, and D. Rugar. *Science*, 339:558, 2013.
  - [12] T. Staudacher, F. Shi, S. Pezzagna, J. Meijer, J. Du, C. A. Meriles, F. Reinhard, and J. Wrachtrup. *Science*, 339:561, 2013.
  - [13] M. Loretz, S. Pezzagna, J. Meijer, and C. L. Degen. *Appl. Phys. Lett.*, 104:033102, 2014.
  - [14] C. Müller, X. Kong, J.-M. Cai, K. Melentijevi, A. Stacey, M. Markham, D. Twitchen, J. Isoya, S. Pezzagna, J. Meijer, J. F. Du, M. B. Plenio, B. Naydenov, L. P. McGuinness, and F. Jelezko. *Nat. Commun.*, 5:4703, 2014.
  - [15] J. D. A. Wood, D. A. Broadway, L. T. Hall, A. Stacey, D. A. Simpson, J.-P. Tetienne, and L. C. L. Hollenberg. *Phys. Rev. B*, 94:155402, 2016.
  - [16] A. Wickenbrock, H. Zheng, L. Bougas, N. Leefer, S. Afach, A. Jarmola, V. M. Acosta, and D. Budker. *Appl. Phys. Lett.*, 109:053505, 2016.
  - [17] L. T. Hall, P. Kehayias, D. A. Simpson, A. Jarmola, A. Stacey, D. Budker, and L. C. L. Hollenberg. *Nat. Commun.*, 7:10211, 2016.
  - [18] H.-J. Wang, C. S. Shin, S. J. Seltzer, C. E. Avalos, A. Pines, and V. S. Bajaj. *Nat. Commun.*, 5:4135, 2014.
  - [19] A. Dreau, J.-R. Maze, M. Lesik, J.-F. Roch, and V. Jacques. *Phys. Rev. B*, 85:134107, 2012.
  - [20] H.-J. Wang, C. S. Shin, C. E. Avalos, S. J. Seltzer, D. Budker, A. Pines, and V. S. Bajaj. *Nat. Commun.*, 4:1940, 2013.
  - [21] H. Clevenson, E. H. Chen, F. Dolde, C. Teale, D. Englund, and D. Braje. *Phys. Rev. A*, 94:021401(R), 2016.
  - [22] S. V. Anishchik and K. L. Ivanov. *Phys. Rev. B*, 96:115142, 2017.
  - [23] D. A. Broadway, J. D. A. Wood, L. T. Hall, A. Stacey, M. Markham, D. A. Simpson, J.-P. Tetienne, and L. C. L. Hollenberg. *Phys. Rev. Appl.*, 6:064001, 2016.
  - [24] V. Ivady, K. Szasz, A. L. Falk, P. V. Klimov, D. J. Christle, E. Janzn, I. Abrikosov, D. D. Awschalom, and A. Gali. *Phys. Rev. B*, 92(11):115206, 2015.
  - [25] J. R. Maze, A. Gali, E. Togan, Y. Chu, A. Trifonov, E. Kaxiras, and M. D. Lukin. *New J. Phys.*, 13:025025, 2011.
  - [26] M. Negyedi, J. Palots, B. Gyre, S. Dzsaber, S. Kollarics, P. Rohringer, T. Pichler, and F. Simon. *Rev. Sci. Instrum.*, 88:013902, 2017.
  - [27] M. W. Doherty, N. B. Manson, P. Delaney, and L. C. L. Hollenberg. *New J. Phys.*, 13:025019, 2011.
  - [28] D. Lee, K. W. Lee, J. V. Cady, P. Ovartchaiyapong, and A. C. Bleszynski Jayich. *Journal of Optics*, 19(3):033001, 2017.
  - [29] D. Budker, D. F. Kimball, and D. P. DeMille.
  - [30] M. Auzinsh, D. Budker, and S. Rochester. *Optically Polarized Atoms, Understanding light-atom interactions*. Oxford University Press, 2010.
  - [31] E. Jones, T. Oliphant, P. Peterson, et al. SciPy: Open source scientific tools for Python. <http://www.scipy.org/>, 2001.
  - [32] X.-F. He, N. B. Manson, and P. T. H. Fisk. *Phys. Rev. B*, 47:8809, 1993.
  - [33] G. D. Fuchs, V. V. Dobrovitski, R. Hanson, A. Batra, C. D. Weis, T. Schenkel, and D. D. Awschalom. *Phys. Rev. Lett.*, 101:117601, 2008.
  - [34] V. Jacques, P. Neumann, J. Beck, M. Markham,

- D. Twitchen, J. Meijer, F. Kaiser, G. Balasubramanian, F. Jelezko, and J. Wrachtrup. *Phys. Rev. Lett.*, 102:057403, 2009.
- [35] B. Smeltzer, J. McIntyre, and L. Childress. *Phys. Rev. A*, 80:050302, 2009.
- [36] A. Gali. *Phys. Rev. B*, 80:241204, 2009.
- [37] B. Smeltzer, L. Childress, and A. Gali. *New J. Phys.*, 13:025021, 2011.
- [38] R. Fischer, A. Jarmola, P. Kehayias, and D. Budker. *Phys. Rev. B*, 87:125207, 2013.